

# Impact of Electrode Architecture on Electrochemical Performance of Aqueous Processed, High-Loaded Lithium-Ion Battery Cathodes

Felix Nagler,<sup>[a]</sup> Andreas Flegler,<sup>[a]</sup> and Guinevere A. Giffin<sup>\*[a, b]</sup>

This study compares two electrode architectures, one with a porous carbon current collector (PC) and the other with a state-of-the-art aluminum foil current collector (AF). The results show that the porous carbon outperforms the aluminum foil at high loadings ( $\sim 8 \text{ mAh/cm}^2$ ) during cycling, likely due to better adhesion. The characterization methods used in the study include electrochemical cycling, electrochemical impedance spectroscopy (EIS), galvanostatic intermittent titration technique (GITT), and scanning electron microscopy (SEM). These methods provide insight into the performance of the two electrode architectures and allow for a comprehensive comparison between them. The findings of this study indicate that the use of porous carbon as a current collector can lead to improved performance in high-loading electrode applications, making it a promising alternative to traditional aluminum foil current collectors.

## Introduction

Lithium-ion batteries (LIB) are widely used in energy storage applications due to their outstanding energy density.<sup>[1,2]</sup> Despite the fact that the energy density of LIBs has nearly tripled over the last decades,<sup>[3]</sup> there is still a growing demand for LIBs with even higher energy densities, e.g., to improve the range of battery electric vehicles (BEV).<sup>[2,4]</sup> One way to do so, without changing the cell chemistry, is to increase the electrode loading. This reduces the amount of electrochemically inactive materials such as current collectors or separators and increases the amount of the electrode active material.<sup>[5–7]</sup> The state-of-the-art cathode architecture uses an aluminum foil as current collector, upon which the cathode composite gets coated.<sup>[7–10]</sup> However, an increase in cathode thickness, in this architecture, is reported to be problematic. The mechanical integrity during drying and cycling, as well as the poor rate performance limit the performance and the lifetime.<sup>[4,6–8,11–13]</sup> Hence, the areal capacity of this cathode architecture is limited to values around  $3 \text{ mAh/cm}^2$  in commercial use.<sup>[14,15]</sup> Attempts to overcome these limitations have included the usage of two dimensional meshes and foams<sup>[16–19]</sup> or even three dimensional porous structures<sup>[20–26]</sup> as cathode current collectors. The higher surface

area of these materials should enhance the adhesion between the cathode composite and the current collector, and hence, the mechanical stability.<sup>[6,14]</sup> Furthermore, the continuous network of electrically conductive current collector improves the rate performance due to a reduced electrical resistance within the electrode.<sup>[6,17,24,27]</sup> In this work, a cathode architecture using a porous carbon structure as a current collector is compared to the state-of-the-art cathode architecture using aluminum foil. For both,  $\text{LiNi}_{0.6}\text{Co}_{0.2}\text{Mn}_{0.2}\text{O}_2$  (NCM622) was used as the active material, along with aqueous electrode processing, which reduces the environmental impact and costs of the LIB production by the elimination of the toxic and costly N-methyl-2-pyrrolidone (NMP).<sup>[28–33]</sup> The infiltration process for the porous carbon structure is further designed to be scalable to a roll-to-roll process. Therefore, a commercially available material (ECM80 (SIGRACET®, SGL carbon)) is used and an infiltration additive (IA) is added to the aqueous slurry to ensure a fast and homogeneous infiltration process. Simplicity and scalability are very important factors if novel electrode manufacturing processes are to be considered as an alternative to the well-established process of cathode manufacturing via slurry casting.<sup>[34]</sup> To the best of the authors knowledge, this was not a primary concern of the previous studies using porous carbon structures as cathode current collectors.<sup>[20–23]</sup> In these studies, in general, at least one step in production was difficult to scaleup, e.g., long heat treatments under nitrogen or argon atmosphere or the usage of a vacuum assisted infiltration. The challenging steps from fabrication are summarized in Table 1 and further discussed in the results.

## Results and Discussion

To study the role of the cathode architecture on the electrochemical performance, electrodes with several loadings were prepared, as summarized in Table 2. The loadings for the AF

[a] F. Nagler, Dr. A. Flegler, Dr. G. A. Giffin  
Fraunhofer R&D Center Electromobility  
Fraunhofer Institute for Silicate Research  
Neuerplatz 2, 97082 Würzburg (Germany)  
E-mail: guinevere.giffin@isc.fraunhofer.de

[b] Dr. G. A. Giffin  
Chair of Chemical Technology of Materials Synthesis  
Julius-Maximilians-University Würzburg  
Röntgenring 11, 97070 Würzburg (Germany)

 Supporting information for this article is available on the WWW under  
<https://doi.org/10.1002/batt.202300063>

 © 2023 The Authors. *Batteries & Supercaps* published by Wiley-VCH GmbH.  
This is an open access article under the terms of the Creative Commons Attribution License, which permits use, distribution and reproduction in any medium, provided the original work is properly cited.

**Table 1.** Performance and production information of different high loaded cathodes using porous carbon structures as current collector.

Current collector	Active material	Current density [mA/cm <sup>2</sup> ]	Cycles	Areal loading [mAh/cm <sup>2</sup> ]	NMP in production	Scalable process possible?	Source
Graphene foam	LFMP	2.5	500	2.5	No	No: Cathode composite has to be annealed under N <sub>2</sub> for 5 h at 700 °C	[23]
Carbon foam	LFP	2	140	5.0	No	No: Carbonize epoxy in Ar for 2 h @ 600 °C	[21]
CNT based porous structure	LFP	2	150	3.0	No	No: Freeze dryer at 24 h @ -47 °C to dry cathode	[24]
Layered porous carbon sheets	NCM111	1.2	100	12	Yes	No: layer by layer vacuum filtration and long drying over night	[22]
Commercial porous carbon fiber network	NCM622	2	50	8.4	No	Yes	This work
				30			
				12.4			

**Table 2.** Slurry compositions, calculated porosities, measured thicknesses, mass loadings and areal loadings of processed cathodes and sample abbreviations. Areal loading is calculated using the discharge capacity of the 6<sup>th</sup> cycle at 0.2 mA/cm<sup>2</sup>.

Current collector	Slurry composition	Porosity/Thickness	Mass loading [mg/cm <sup>2</sup> ]	Areal loading [mAh/cm <sup>2</sup> ]	Sample name
Aluminum foil "AF"	92 wt% NCM622 4 wt% CMC 4 wt% C65	50%/60 µm 50%/150 µm 50%/250 µm	12.08 ± 0.21 29.40 ± 0.55 47.45 ± 1.44	2.11 ± 0.04 5.23 ± 0.10 8.69 ± 0.26	AF <sub>low</sub> AF <sub>medium</sub> AF <sub>high</sub>
ECM80	89 wt% NCM622	85%/700 µm	28.49 ± 2.91	4.60 ± 0.47	PC <sub>medium</sub>
SIGRACET® SGL "PC"	4 wt% CMC 4 wt% C65 3 wt% BYK3450 92 wt% NCM622 4 wt% CMC 4 wt% C65	77%/700 µm 82%/1000 µm 69%/700 µm 84%/1000 µm	49.56 ± 3.12 55.98 ± 1.35 70.80 ± 5.04 40.44 ± 4.17	8.39 ± 0.53 9.67 ± 0.23 12.42 ± 0.88 7.43 ± 0.77	PC <sub>high</sub> PC <sub>very-high II</sub> PC <sub>very-high</sub> PC <sub>high, w/o-IA</sub>

and PC cathodes are in the range of 2.1–8.7 mAh/cm<sup>2</sup> and 4.6–12.4 mAh/cm<sup>2</sup>, respectively. In addition, a cathode without the IA was prepared to probe the influence of the additive on the electrochemical performance.

The distribution of the cathode components in the PC substrate was examined with SEM cross-section images, as shown in Figure 1. The pristine PC structure (Figure 1a) consists of interwoven carbon fibers and has an overall thickness of about 700 µm. The porosity of the sheet was calculated to be around 95% (calculation shown in Supporting Information). The cross sections of an infiltrated PC (Figure 1b-d) show that

the cathode composite is attached to the carbon fibers of the PC structure. The NCM particles (bright particles) are distributed homogeneously over the entire thickness of the cathode. The black spots, which can be seen in Figure 1d), are most likely holes, which were not filled with the epoxy resin during preparation. The cross sections of the AF cathodes are shown in Figure S3, for comparison purposes, in the supplementary information. To see the influence of the cathode architecture on the electrochemical performance and to find out the rate capability for both architectures a current density test with current densities of 0.2, 0.5, 1.0, 2.0 and 3.0 mA/cm<sup>2</sup> is performed. The resulting discharge capacities are shown in Figure 2.

First, it can be seen that the discharge capacities of the PC cathodes are generally somewhat lower than that of the AF cathodes. At similar loading and same current density of 0.2 mA/cm<sup>2</sup> the PC<sub>high</sub> show a discharge capacity of 170 mAh/g, whereas the AF<sub>high</sub> show 182 mAh/g. The most obvious possible reason could be the higher thickness of the cathodes (AF<sub>high</sub> ~ 250 µm, PC<sub>high</sub> ~ 700 µm), which should result in longer diffusion paths due to the higher tortuosity of the cathodes.

However, when testing a PC cathode, which was infiltrated without the usage of the IA (PC<sub>high, w/o-IA</sub>), no further polarization is observed in comparison to similar loaded AF cathodes. The voltage curves are shown in Figure 2b). Thus, the higher thickness does not seem to be the reason for the additional polarization, but rather the usage of the IA. It is possible that IA is forming some kind of surface film on the NCM622 surface, which causes the additional polarizations, and thus the lower capacity. SEM was used in an attempt to visualize such a

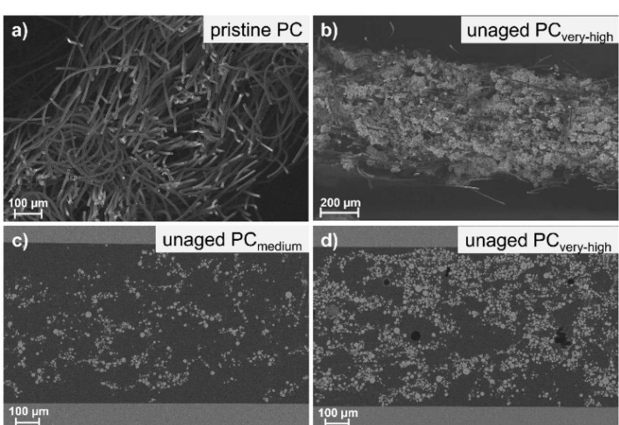


**Figure 1.** SEM cross-section images of a) pristine PC structure, b) infiltrated PC<sub>very-high</sub> with loading of (12.42 ± 0.88) mAh/cm<sup>2</sup>. SEM IM cross-section images of infiltrated PC<sub>medium</sub> and PC<sub>very-high</sub> with a loadings of c) (4.60 ± 0.47) mAh/cm<sup>2</sup> and d) (12.42 ± 0.88) mAh/cm<sup>2</sup>, respectively.

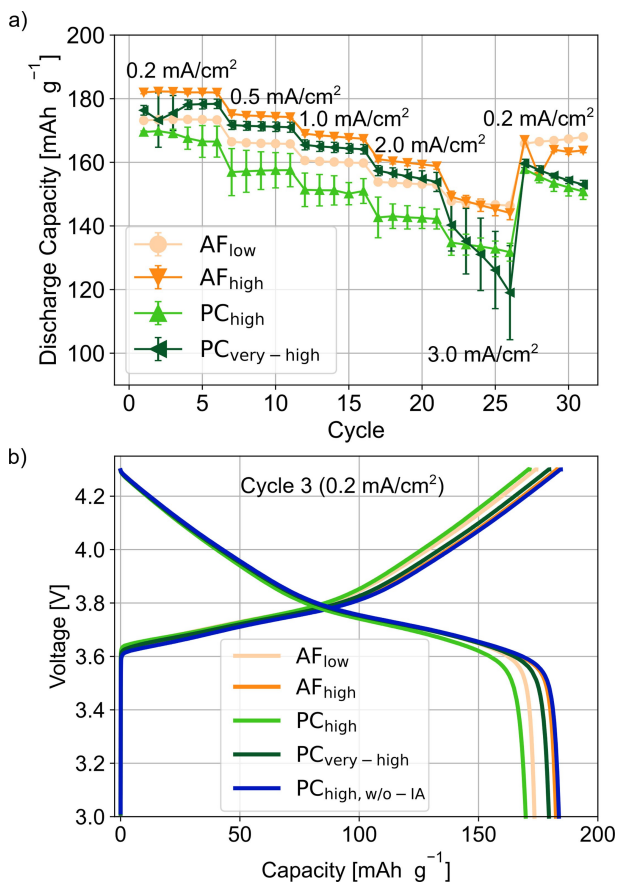


**Figure 2.** a) Mean discharge capacity and standard deviation of three cells at different current densities, b) voltage profiles of representative cell from each sample of cycle 3, with a current density of  $0.2 \text{ mA}/\text{cm}^2$ .

surface layer with the IA. In Figure S2, a comparison of NMC with and without the IA is shown (i.e., a NMC622 particle from a PC<sub>medium</sub> and PC<sub>high, w/o-IA</sub>). Darker areas are visible at the particle surface from PC<sub>medium</sub>, which could be caused by the IA. Further the current density test shows that the discharge capacities increase with increasing loading (see Figure 2a). At a current density of  $0.2 \text{ mA}/\text{cm}^2$ , the discharge capacity increases from  $173 \text{ mAh/g}$  to  $182 \text{ mAh/g}$  for AF<sub>low</sub> to AF<sub>high</sub>, and from  $170 \text{ mAh/g}$  to  $178 \text{ mAh/g}$  for the PC<sub>high</sub> to PC<sub>very-high</sub>, respectively. This trend can be explained by the fact that the electrochemically active surface increases with higher loading, since the current density is set in relation to the electrode area and not surface area of the NCM622 particles. This results in a higher polarization (Figure 3b) in the cells with the lower loading, since the same current is applied to a smaller active material surface area. This leads to slightly lower discharge capacities per gram of active material for the lower loaded cathodes.

This trend holds up to a current density of  $2.0 \text{ mA}/\text{cm}^2$ . At a current density of  $3.0 \text{ mA}/\text{cm}^2$ , capacity fading occurs for some of the cathodes (e.g., PC<sub>very-high</sub> and AF<sub>high</sub>), which is most likely an effect related to the lithium metal counter electrode (CE).

As reported in literature, the interplay of current density, areal capacity and the number of cycles defines the morphol-

ogy of the lithium metal CE.<sup>[35–37]</sup> It is possible that even the relatively small current density of  $3.0 \text{ mA}/\text{cm}^2$  leads to the formation of a thick and high resistance layer of dead and mossy lithium.<sup>[38]</sup>

Based on a simple calculation, the thickness of the lithium plated with the high areal capacity cathodes (i.e., PC<sub>very-high</sub>), is theoretically greater than  $60 \mu\text{m}$  (expansion of  $\sim 4.9 \mu\text{m}$  per  $\text{mAh}/\text{cm}^2$  calculated by using Faraday's law, assuming the deposition of a dense, homogeneous lithium layer<sup>[39]</sup>). However, the real expansion is expected to be much higher. A recent publication showed an expansion of  $7.9 \mu\text{m}$  per  $\text{mAh}/\text{cm}^2$  during stripping and a contraction of  $5.4 \mu\text{m}$  per  $\text{mAh}/\text{cm}^2$  at a current density of  $2.0 \text{ mA}/\text{cm}^2$  and a CE (LTO, lithium titanate) loading of ca.  $2.0 \text{ mAh}/\text{cm}^2$  with a similar carbonate-based electrolyte.<sup>[38]</sup> The difference in dilation between the two half cycles was  $2.5 \mu\text{m}$  per  $\text{mAh}/\text{cm}^2$ , which was associated with deposition of mossy lithium along with the build-up of solid electrolyte interphase, followed by the formation of dead lithium in the subsequent half cycle. Given that the amount of lithium cycled is almost six times higher in this case, the irreversible dilation is expected to be significant. The resistance associated with this layer is most likely the cause of the higher polarization, particularly at  $3.0 \text{ mA}/\text{cm}^2$  (Figure 3d), which results in the capacity fading. The challenge associated with the CE is also the reason why a C-rate test is not suitable to compare the cathodes with different loadings. The higher-loading cathodes would suffer much more from the instability on the lithium side, since the current density increases for higher loaded electrodes if the C-rate is kept constant. It was decided that the maximum current density for further cycling would be  $2.0 \text{ mA}/\text{cm}^2$ . All cathodes show, at least initially, a stable cycling performance at this current density (see also Figure S4).

To further study the resistances within the cathodes, EIS measurements were performed at cell voltages of  $3.8 \text{ V}$  ( $\sim 50\%$  state-of-charge (SOC)) and  $4.3 \text{ V}$  ( $\sim 100\%$  SOC). The Nyquist plots, the equivalent circuits used for fitting and the fitting results are shown in Figure 3. For clarity, only the data of a few samples are shown. All data and fitted values are summarized in Figure S5 and Table S2. At a cell voltage of  $3.8 \text{ V}$  (Figure 4a), several features can be seen in the impedance spectra of the cells with both types of cathodes. The high frequency intercept is caused by the ohmic resistances within the cell ( $R_{IR}$ ).

The first semicircle at high frequencies can be associated with the electrical conductivity within the cathode ( $R_e$ ). The semicircle at mid frequencies can be attributed to the solid electrolyte interphase ( $R_{SEI}$ ). The semicircle at low frequencies can be linked to the charge transfer resistance ( $R_{CT}$ ).<sup>[28,40–42]</sup> For the EIS measurement at  $4.3 \text{ V}$  (see Figure 3b), the same model can be used for the AF cathodes. For the PC cathodes an additional semicircle at even lower frequencies than that linked to the charge transfer can be observed ( $R_{Th}$ ). Based on these features, the equivalent circuit models shown in Figure 3c) and d) were used to fit the data collected at  $3.8 \text{ V}$  and  $4.3 \text{ V}$ , respectively.

As it can be seen from the fitted values presented in Figure 3e) and f), the high frequency resistance associated with

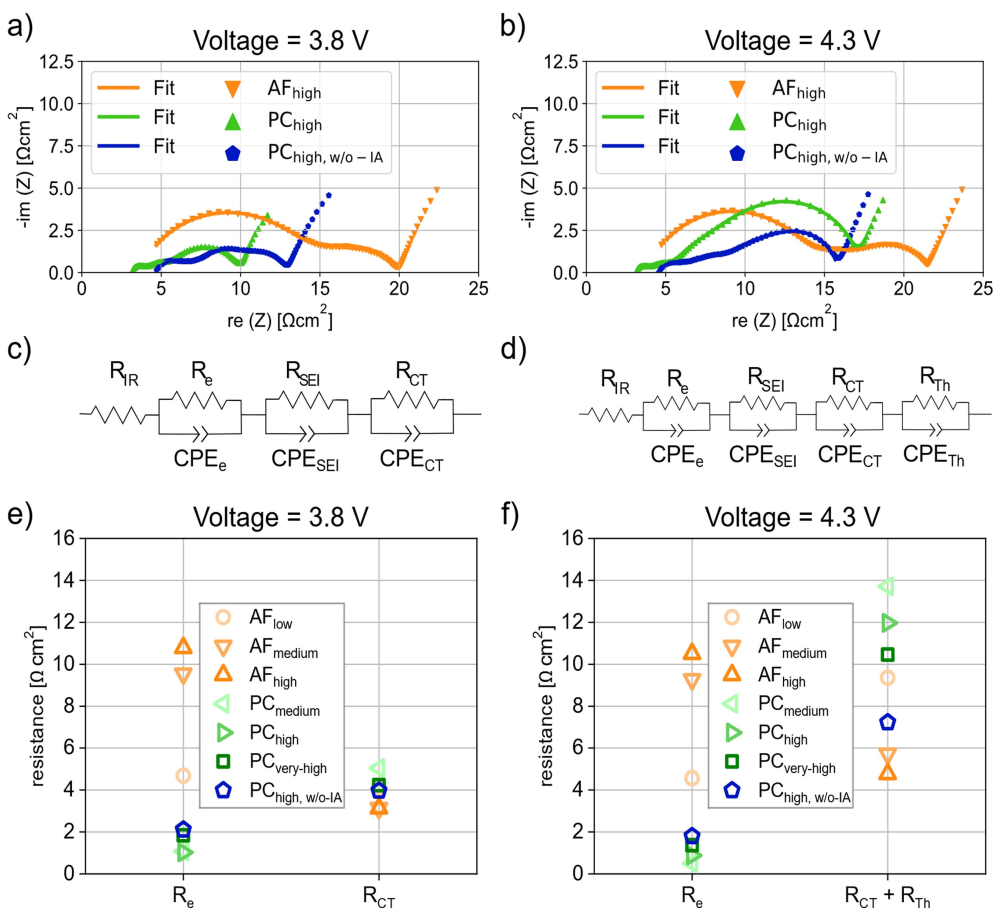


**Figure 3.** a) Nyquist plot of EIS measurements at cell voltage of 3.8 V, b) Nyquist plot of EIS measurements at cell voltage of 4.3 V, c and d) the equivalent circuits for fitting EIS data shown in parts (a) and (b); e and f) fit values from EIS data.

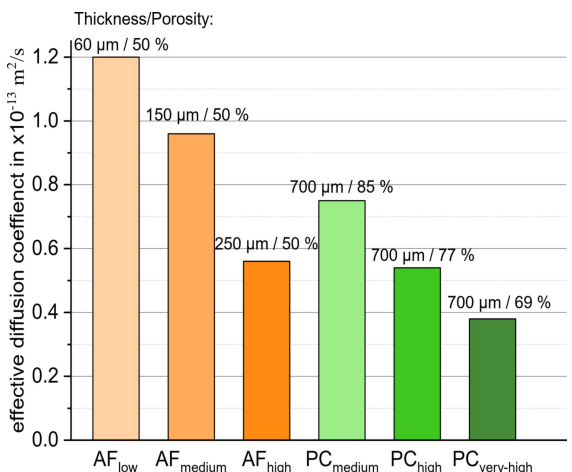


**Figure 4.** Effective diffusion coefficient calculated with GITT data.

the electrical resistance within the cathode  $R_e$  is much lower for the PC cathodes compared to the AF cathodes due to the continuous carbon network. The PC cathodes show  $R_e$  values below approximately  $2.0 \Omega \text{cm}^2$ . In contrast, the AF cathodes show  $R_e$  values between  $4.5$  and  $10.5 \Omega \text{cm}^2$  for  $\text{AF}_{\text{low}}$  to  $\text{AF}_{\text{high}}$ . The increasing electrical resistance with loading of the AF

cathodes latter can be explained by the higher cathode thickness (see Table 2).

The resistances associated with the charge transfer  $R_{\text{CT}}$  increase for the AF cathodes with increasing SOC. The  $R_{\text{CT}}$  increases from  $3.1$  to  $4.8 \Omega \text{cm}^2$  and from  $4.2$  to  $9.4 \Omega \text{cm}^2$  (at  $3.8 \text{ V}$  and  $4.3 \text{ V}$ , respectively) for  $\text{AF}_{\text{high}}$  to  $\text{AF}_{\text{low}}$ . The increase of  $R_{\text{CT}}$  from medium to high SOCs is consistent with results reported in the published literature.<sup>[43-45]</sup> According to Schipper et al., a possible reason could be a partial layered to spinel phase transformation within the  $\text{LiNi}_{0.6}\text{Co}_{0.2}\text{Mn}_{0.2}\text{O}_2$  (NCM622) structure, which would cause a higher  $R_{\text{CT}}$ .<sup>[45]</sup> Furthermore, the trend of higher loading electrodes having a lower  $R_{\text{CT}}$  has been reported by Ogihara et al.<sup>[46]</sup> The reason for this trend is that the NCM622 surface area increases with increasing cathode thickness. For the PC cathodes, which have a thickness of about  $700 \mu\text{m}$  but different porosities (see Table 2)  $R_{\text{CT}}$  increases with increasing porosity for the measurements at  $3.8 \text{ V}$  ( $\text{PC}_{\text{medium}}$ :  $5.0 \Omega \text{cm}^2$ ,  $\text{PC}_{\text{very-high}}$ :  $4.2 \Omega \text{cm}^2$ ). Kim et al. saw the same trend while varying the electrode porosity and concludes that the electrical resistance increases with higher porosity, which leads to higher  $R_{\text{CT}}$ .<sup>[27]</sup> Only  $\text{PC}_{\text{high}, \text{w/o-IA}}$  does not follow this trend, and has a slightly lower  $R_{\text{CT}}$  of  $4.0 \Omega \text{cm}^2$ . This could be associated with the absence of the IA in the electrode composition, which maybe forming a blocking film on the NCM particle surface.

For EIS-measurements at 4.3 V, the additional semicircle located at low frequencies complicates the interpretation of  $R_{CT}$  for the PC cathodes. The reason for the additional feature might be associated with higher cathode thickness, as it also appears in the sample without the IA (see Figure 3b)). This hypothesis is supported by the fact that cathodes using an identical manufacturing process, but with another porous carbon structure, i.e., the gas diffusion sheets, that has a lower thickness, do not have an additional feature at a cell voltage of 4.3 V (see EIS data in Figure S6). Side reactions involving the PC structure can also be excluded, since a cyclic voltammetry (CV) measurement of the blank PC structure does not show any significant features at in this voltage range (see supplementary Figure S7). Based on all of the arguments presented above, it can be concluded that the additional resistance is most likely related to the thickness. Since the  $R_{Th}$  appears in a similar frequency region to the  $R_{CT}$ , the resistances are hard to separate during fitting. Therefore, only the sum of both  $R_{CT} + R_{Th}$  is used for interpretation. As can be seen in Figure 3f), the  $PC_{high, w/o-IA}$  has the smallest  $R_{CT} + R_{Th}$  of all PC cathodes ( $7.2 \Omega \text{cm}^2$ ). Furthermore, the  $R_{CT} + R_{Th}$  decreases with increasing loading of the PC cathodes, i.e.,  $PC_{medium}$  has the highest  $R_{CT} + R_{Th}$  value of  $13.7 \Omega \text{cm}^2$ . The higher active material surface area with higher mass loading is likely responsible for this result.<sup>[46]</sup> This trend explains the voltage curves in Figure 2(b), where the  $PC_{high, w/o-IA}$  exhibits similar polarization as the AF cathodes. Thus, the additional polarization of the other PC cathodes at high cell voltages is most likely caused by the IA, as is evident from the higher  $R_{CT} + R_{Th}$ . As mentioned above, it is possible that the IA is forming a surface layer on the NCM particles, which hinder the charge transfer. Therefore, a tradeoff has to be made between a fast infiltration process and additional polarizations for the PC cathodes. Depending on the chemical nature of the IA, attempts may be made to remove it with an additional heating step during drying of the cathodes.

From the fitted data in Figure S5 it can be seen that the resistances attributed to the ohmic resistances  $R_{IR}$  are between  $2.0$  and  $4.0 \Omega \text{cm}^2$  for most of the AF and PC cathodes. They are also relatively independent of SOC. Only the cell with the  $PC_{high, w/o-IA}$  cathode has a slightly higher  $R_{IR}$  ( $\sim 4.5 \Omega \text{cm}^2$ ), which may be related to the fact that this cathode was not calendered and therefore has a higher thickness ( $\sim 1000 \mu\text{m}$ ). Furthermore, the resistances attributed to the SEI  $R_{SEI}$  are also consistently low for all cells in the range of  $1.0$  to  $2.5 \Omega \text{cm}^2$  and do not vary significantly with SOC.

To get a better understanding of the influence of the electrode architecture on the Li-ion diffusion, the effective diffusion coefficients  $D_{eff}$  were determined by performing GITT measurements. The calculated  $D_{eff}$  for the various cathodes are presented in Figure 4. Since the  $D_{eff}$  is more or less constant over the analyzed voltage range of  $3.9$  to  $4.2 \text{ V}$ , only one value is presented per cathode. The calculation method introduced by Weppner and Huggins was used.<sup>[47]</sup> An exemplary evaluation of a GITT pulse is shown in Figure S8. The effective diffusion coefficient  $D_{eff}$ , as shown in Figure 4, decreases with increasing thickness from  $1.20$  to  $0.55 \times 10^{-13} \text{ m}^2/\text{s}$  for  $AF_{low}$  to  $AF_{high}$ . For the PC cathodes, the effective diffusion coefficient decreases

with decreasing porosity from  $0.75$  to  $0.38 \times 10^{-13} \text{ m}^2/\text{s}$  for the  $PC_{medium}$  to  $PC_{high}$ . The effective diffusion coefficient  $D_{eff}$  of the cathodes is influenced by the solid-state diffusion within the active material particles as well as from the ionic transport in the electrolyte. Since all cathodes are using the same materials (active material and electrolyte), the only difference should be the interplay of cathode porosity and tortuosity which defines the effective diffusion length of the lithium ions. For the AF cathodes, where the porosity is constant, the tortuosity increases with increasing cathode thickness leading to longer diffusion pathways and hence to lower  $D_{eff}$ . For the PC cathodes, the porosity decreases with increasing loading, which then also should lead to overall higher diffusion pathways and hence to lower  $D_{eff}$ . Although  $AF_{low}$  is about  $11$  times thinner than the PC cathodes, the  $D_{eff}$  is only  $1.5$  to  $3$  times higher. This most likely due to the much higher porosity of the PC cathodes, resulting in similar diffusion pathways compared to the AF cathodes.

For testing the cycling performance and stability, a cyclization test was performed. The discharge capacities are presented in Figure 5. As seen in the current density test (Figure 2a), the same trend in the initial discharge capacities holds true in the cycling test (Figure 5a). The discharge capacities increase with loading for both the AF and PC

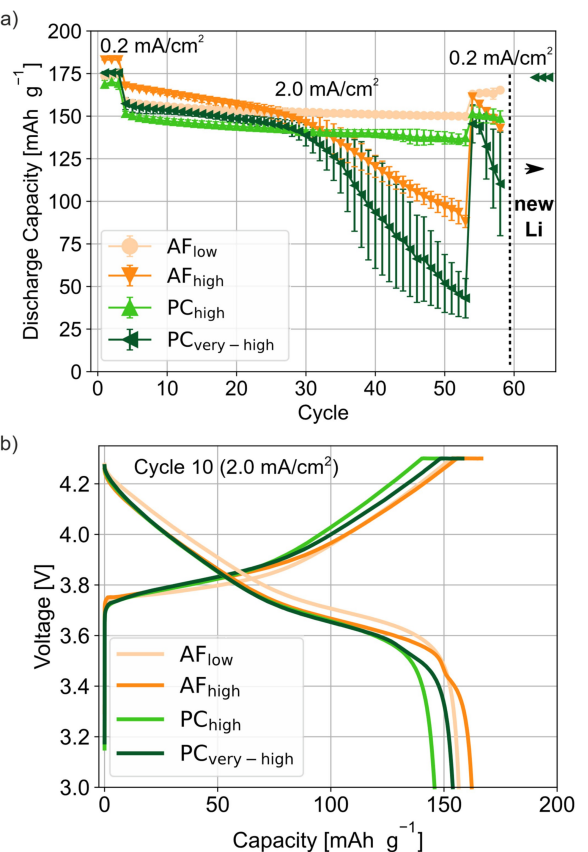


**Figure 5.** a) Discharge capacity against cycle number (dashed line indicates that the cells were opened, and the cathodes were built into new cells with fresh lithium metal and separator) the error bar indicates the standard deviation of three measured cells, b) voltage curves of a representative cell of each sample at cycle 10.

cathodes, although the discharge capacities for the PC cathodes are lower than those of the AF cathodes. For the AF cathodes, only  $\text{AF}_{\text{low}}$  shows a reasonably stable cycling behavior at the current density of  $2.0 \text{ mA/cm}^2$ . The capacity retention is 94.4% after 50 cycles (i.e., a capacity decrease from 158.8 to  $149.9 \text{ mA/g}$ ). For  $\text{AF}_{\text{high}}$ , which has a loading of  $8.7 \text{ mAh/cm}^2$ , capacity fading can be observed at around cycle 30. Also,  $\text{AF}_{\text{medium}}$ , with a loading of  $5.2 \text{ mAh/cm}^2$  shows capacity fading starting from around 40 (data shown in Figure S9). The PC cathodes can be cycled stably up to a loading of  $8.4 \text{ mAh/cm}^2$ .  $\text{PC}_{\text{high}}$  shows a capacity retention of 90.6% after 50 cycles at  $2.0 \text{ mA/cm}^2$  (151.5 to  $137.4 \text{ mAh/g}$ ). The remaining capacity in the 50<sup>th</sup> cycle at  $2.0 \text{ mA/cm}^2$  is equal to an areal loading of around  $6.57 \text{ mAh/cm}^2$ . In comparison, the  $\text{AF}_{\text{low}}$  has an areal loading of  $1.79 \text{ mAh/cm}^2$  at the 50<sup>th</sup> cycle at  $2.0 \text{ mA/cm}^2$ . At higher electrode loadings, i.e.,  $\text{PC}_{\text{very-high}}$ , some capacity fading occurs during cycling, starting around cycle 25.

To further investigate the origin of the capacity fading for both cathode architectures, the cells were opened after the cycling test. In Figure 6, pictures of the aged  $\text{AF}_{\text{low}}$  and  $\text{AF}_{\text{high}}$  cathodes as well as those of the aged  $\text{PC}_{\text{high}}$  and  $\text{PC}_{\text{very-high}}$  cathodes are presented. As Figure 6a) and c) shows, the  $\text{AF}_{\text{low}}$  seems to remain intact and shows no major defects or areas with delamination can be detected. In contrast, the  $\text{AF}_{\text{high}}$  shows areas of delamination, where the majority of the cathode material is attached to the glass fiber separator (see Figure 6d). In addition, the cross section of the remaining part of the electrode, where the cathode material stays attached to the aluminum foil, shows some cracks and the start of delamination from the aluminum foil (see Figure 6b)). Therefore, it is most likely that delamination processes, which occur throughout cycling, induce additional polarization, which then lead to the observed capacity fading with the higher-loading AF cathodes. The cause of the more significant delamination of the higher-loading AF cathodes might be reduced adhesion of the cathode composite to the aluminum foil current collector due to increased crack formation during drying and/or cycling of the electrodes.<sup>[6,7,9,48,49]</sup> The lithium metal CE could also contrib-

ute to the observed polarizations, as described above. However, it is very unlikely to be the sole origin of the polarization for the AF cathodes. Although there is certainly mossy and dead lithium present on anode side, the PC cathode can be stably cycled up to a loading of  $8.4 \text{ mAh/cm}^2$  for 50 cycles at the same current density of  $2.0 \text{ mA/cm}^2$ , while capacity fading is already observed for the AF with an areal loading of  $5.2 \text{ mAh/cm}^2$  after around 40 cycles at  $2.0 \text{ mA/cm}^2$  (see Figure S9). Hence, the lithium CE should not be the main cause for the observed capacity fading at the AF cathodes. For the PC cathodes, no major changes in the microstructure of the electrode can be observed and the active material particles are still attached to the carbon structure (see Figure 6e) and f)). Since the capacity fading for the PC cathodes starts earlier for the  $\text{PC}_{\text{very-high}}$  than for the  $\text{PC}_{\text{very-high-II}}$  which has a bit reduced loading of  $9.7 \text{ mAh/cm}^2$  (data in Figure S9), the lithium metal CE could be the main reason for the capacity fading. To further investigate this point, some of the  $\text{PC}_{\text{very-high-II}}$  and  $\text{PC}_{\text{very-high}}$  electrodes were recovered from the original cells and subsequently cycled against a new lithium metal CE. In Figure 5 (data after the dashed line), the PC cathodes nearly return to their initial capacity, which supports the idea that the observed capacity fading arises primarily from the lithium metal CE. Therefore, it is possible that even higher loading PC cathodes can be stably cycled if the degradation at the CE could be controlled.

The performances of other cathodes using a porous carbon structure as current collector are summarized in Table 1. Zhao et al. showed stable cycling of a carbon cathode structure with vertically-aligned channels for 500 cycles with loading around  $2.5 \text{ mAh/cm}^2$  at  $2.5 \text{ mA/cm}^2$ .<sup>[23]</sup> Chen et al. reported stable cycling of 3D carbon cathodes with a loading of around  $5 \text{ mAh/cm}^2$  for 140 cycles at  $2.0 \text{ mA/cm}^2$ .<sup>[21]</sup> Kuang et al. shows a conductive cellulose network with a stable cycling of 150 cycles at a loading of around  $3.0 \text{ mAh/cm}^2$  at  $2.0 \text{ mA/cm}^2$ .<sup>[24]</sup> The best performance is presented by Wu et al., where a stable cycling of a layered-structured, porous cathode with a loading of  $36 \text{ mAh/cm}^2$  for 30 cycles at  $3.6 \text{ mA/cm}^2$  is demonstrated. In that work, a special electrolyte formulation was used to help build a more stable SEI on the lithium CE to achieve a stable cycling at comparably high loadings and current densities. They further showed the stable cycling of cathodes with  $12 \text{ mAh/cm}^2$  for 100 cycles at  $1.2 \text{ mA/cm}^2$ .<sup>[22]</sup> Compared to these results the performance of the PC cathodes shown in this work is quite competitive (50 cycles with  $8.4 \text{ mAh/cm}^2$  at  $2.0 \text{ mA/cm}^2$ , 30 cycles with  $12.4 \text{ mAh/cm}^2$  at  $2.0 \text{ mA/cm}^2$ ) and the fabrication was comparatively simple. All the other works mentioned above require at least one time consuming annealing step under a nitrogen<sup>[23]</sup> or argon<sup>[21]</sup> atmosphere, a long freeze drying step<sup>[24]</sup> or vacuum-assisted<sup>[22]</sup> infiltration. The production process for the PC cathode in this work should be scalable to a roll-to-roll process. Furthermore, the limit of the areal loading does not seem to have been reached for the PC cathodes, since  $\text{PC}_{\text{very-high}}$  still has a porosity of about 69%. However, it is hard to characterize even higher-loading cathodes in half cells due to the limitations of the lithium CE, as discussed in detail above. Therefore, to explore the loading limits of the PC structure, the switch to full cells is necessary and will be addressed in further

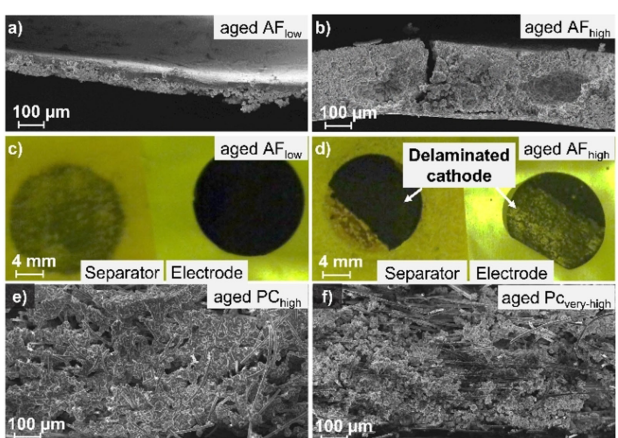


**Figure 6.** SEM cross-section and image of a and c) aged  $\text{AF}_{\text{low}}$ , b and d) aged  $\text{AF}_{\text{high}}$ ; SEM cross-section of e) aged  $\text{PC}_{\text{high}}$ , f) aged  $\text{PC}_{\text{very-high}}$ . The yellowish color in (c and d) comes from the glovebox, which has yellow light.

studies. In this case, the challenge is to also produce anodes with similarly high loadings. The results obtained imply a higher gravimetric energy density with the PC cathodes on the cell level. However, given the high porosity, the volumetric energy density would decrease even at the highest loadings of the PC cathodes investigated here. Hence it is crucial to further reduce the porosity, to not only achieve better gravimetric energy density (i.e., less electrolyte needed) but to also improve the volumetric energy density. State-of-the-art cathodes do have porosities between 20–30%.<sup>[50,51]</sup> Possibilities would be a more extensive calendaring of the cathodes, a further increase of mass loading or the usage of thinner PC structure with similar mass loadings.

## Conclusions

Cathodes with a porous carbon structure as current collector show remarkable performance during cycling with high loadings. To come to this conclusion, PC cathodes with an areal capacity between ca. 5 and 12 mAh/cm<sup>2</sup> were prepared and tested in a half cell configuration with lithium metal as a CE. The PC<sub>high</sub>, with a loading of 8.4 mAh/cm<sup>2</sup> can be stably cycled with a capacity retention of over 90% after 50 cycles at 2.0 mA/cm<sup>2</sup>, whereas the AF cathodes already show capacity fading starting from 5.2 mAh/cm<sup>2</sup>. Cycling cathodes with this high loading range, particularly with higher current densities, is challenging. Therefore, at higher cathode loadings (>8.5 mAh/cm<sup>2</sup>), the lithium metal CE most likely limits the cycling performance and causes capacity fading. The results obtained when replacing the CE with a fresh lithium foil supports this conclusion. In a subsequent study, these challenges will be addressed through the use of a full cell configuration. One further challenge of this work was tailoring the aqueous electrode slurry to allow infiltration of the hydrophobic porous carbon structure and thus an IA was needed. The IA induces additional polarization at high cell voltages, but leads to a much better infiltration behavior. This aspect is particularly important for the next step in this work, which is to address the scalability of the production process.

## Experimental Section

### Electrode processing:

To prepare conventional cathodes on aluminum foil (AF), an aqueous slurry consisting of 92 wt% NCM622 (Umicore S.A., 5557180a), 4 wt% sodium carboxymethyl cellulose (CMC, M<sub>w</sub>~250 000 g mol<sup>-1</sup>, degree of substitution 0.9, Sigma Aldrich Chemie GmbH) as binder and 4 wt% Super C65 (C-NERGY™, Imerys S.A.) as conductive carbon was used. The CMC was dissolved in deionized water over night before adding the NCM622 and the Super C65. The slurry was mixed for 2 h with a Speedmixer (DSC 400.1 Vac-P, Hauschild GmbH & Co. KG). The water amount was adjusted to 120 wt% for the AF<sub>low</sub> slurries or 80 wt% for the AF<sub>medium</sub> and AF<sub>high</sub> slurries in comparison to the solid component. The slurry with 120 wt% water was used to make the AF<sub>low</sub>. The slurry with 80 wt% was used to produce higher loading cathodes on

aluminum foil (AF<sub>medium</sub> and AF<sub>high</sub>). The wet gap size during the doctor blade coating was adjusted to 290 µm, 480 µm and 800 µm for AF<sub>low</sub>, AF<sub>medium</sub> and AF<sub>high</sub> electrodes, respectively. After coating the slurry on aluminum foil, the cathodes were pre-dried for about 1 h at 80 °C before being calendered to a porosity of about 50%. Disc electrodes with a diameter of 16 mm were punched out and further dried under vacuum for 12 h at 110 °C. The properties of the different AF cathodes are summarized in Table 2. In a preliminary screening of different porous structures, an aluminum foam (Sumitomo Electric Europe Ltd), a titanium foam (Xiamen Tmax Battery Equipments Limited) and another porous carbon (CeTech) were tested along with the ECM80. The ECM80 structure enabled the highest loadings and the best infiltration (see Table S3). The cathodes using the porous, carbonaceous structure (PC), ECM80 (SIGRACET®, SGL Carbon SE), were infiltrated with an aqueous slurry consisting of 89 wt% NCM622, 4 wt% CMC, 4 wt% Super C65 and 3 wt% BYK3450 (silicone surfactant, BYK Additives & Instruments) as an infiltration additive. The IA is added to the aqueous slurry to ensure a fast and homogeneous infiltration process into the hydrophobic PC structure by reducing the surface tension. The slurry was mixed for 2 h with a Speedmixer. The water amount was adjusted to 175 wt%, 120 wt% and 80 wt% with respect to the solid components to produce the different cathode loadings. To infiltrate the PC, the aqueous slurry was drop-casted on both sides of the substrate for 2 min each. The amount of the IA was adjusted to have a hydrophilic contact and therefore a good infiltration. Hence, several amounts of the IA were tested by measuring the contact angle of the slurry on the PC structure with a drop shape analyzer (DSA100E, Krüss GmbH). The results of the analysis are shown in Figure S8 in the supplementary information. To see the influence of the IA on the electrochemical performance, a PC cathode without IA was produced using the same formulation as the slurry coated on the PC structure (PC<sub>high, w/o IA</sub>). Without the IA the slurry is very hydrophobic and only infiltrates while getting spread manually with a spatula (see Figure S11). The infiltrated PC cathodes were pre-dried for 1 h at 80 °C. Some of the PC cathodes were calendered to a thickness of about 700 µm. The properties of the cathodes are summarized in Table 2. Subsequently, disc electrodes with a diameter of 16 mm were punched out and dried under vacuum for 12 h at 150 °C. The cathode manufacturing of both the AF and PC cathodes is shown schematically in Figure 7. To understand possible thickness effects of the cathodes, some porous, carbon gas-diffusion sheets (GDS, GDS250 and GDS310, CeTech Co., Ltd.) were used as the current collector. They were processed in the same way as the ECM80. After drying, they had thicknesses of 395 µm (GDS250) and 450 µm (GDS310) and were not calendered.

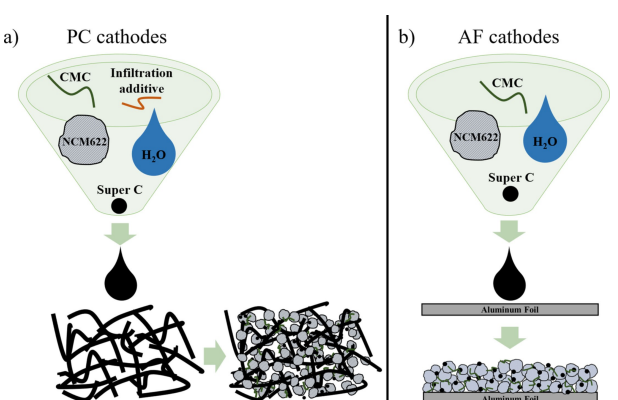


Figure 7. Schematic representation of the cathode manufacturing of a) PC cathodes and b) AF cathodes.

## Cell assembly and electrochemical measurements

The cathodes were tested in half cells against lithium metal (Sigma-Aldrich) on a copper substrate as CE, a glass-fiber separator (Whatman GF/C) and 400 µL of 1 mol/L LiPF<sub>6</sub> in EC/DMC 1:1 wt% / wt% (LP30, BASF SE) as electrolyte. With that all cells certainly have an excess of electrolyte. The lithium metal was scrapped with a ceramic knife to remove the oxide layer. Subsequently, the lithium metal was rolled onto dendritic copper (SE-Cu R360, Schlenk Metallfolien GmbH & Co. KG). The cells were assembled in an argon-filled glovebox (GS-Glovebox, O<sub>2</sub><1.0 ppm, H<sub>2</sub>O<0.1 ppm). Three cells of each cathode batch were prepared for the current-density and cyclization tests in a pouch cells format. Aluminum and nickel-copper tabs (Targray Battery & Energy Storage) were used to contact cathode and anode, respectively. To ensure good contact a stainless-steel spacer was added on each side for the cells with PC cathodes. In the case of some cells, the PC cathodes were recovered after post-mortem analysis and used to build cells with fresh lithium, separator and electrolyte. Current-density and cyclization tests were performed on an electrochemical workstation (Maccor, Series 4000, Maccor Inc.) in the voltage range of 3.0 V to 4.3 V at 25 °C (IPP260, Memmert GmbH + Co. KG). The cells were charged with a constant-current constant-voltage procedure (CCCV) and discharged with a constant-current procedure (CC). The CV-step was terminated at a current of 0.5 mA.

EIS and GITT measurements were performed on a VMP300 galvanostat/potentiostat (BioLogic GmbH). Before measuring the impedance spectra, the cells were cycled three times with a current density of 0.2 mA/cm<sup>2</sup> as a formation step. A CV step of 3 h was applied before the impedance measurements to ensure that the cells were at equilibrium at the various state of charge (SOC). The impedance spectra were obtained by the perturbation of the cells with an AC voltage (amplitude: 5 mV) over the frequency range of 10 mHz to 1 MHz. The GITT measurements were performed after the EIS measurements, on the same cells. The cells were charged from 3.9 V to 4.2 V through the application of 10 min current pulses followed by a relaxation step of 60 min. The data collection rate in the first second after the start and end of each pulse was increased to 5 kHz to determine the IR drop as accurate as possible. A python script was used to identify the relevant potentials E<sub>0</sub> to E<sub>3</sub>, which are needed for the calculation of the effective diffusion coefficient, D<sub>eff</sub>, according to Weppner and Huggins.<sup>[47]</sup> For the EIS and GITT measurements at least two cells were prepared. These were built in ECC-Ref cells (EL-Cell GmbH).

To determine if side reactions involving the current collectors are taking place, CV measurements were conducted on the pristine ECM80 and aluminum foil. Lithium metal was used as the counter electrode with 200 µL of LP30 as electrolyte, in combination with a glass fiber separator with a thickness of 260 µm (Whatman GF/C). The voltage was varied with a step size of 1 mV/s between 3.0 and 5.0 V for three cycles.

## Characterization methods

Cross-sections of the cathodes were investigated by SEM (ZEISS Supra 25, Carl Zeiss Microscopy GmbH). The cross-section preparation was conducted by cutting the cathodes with a scalpel. Some cross-sections were infiltrated with an epoxy resin and gently polished with SiC-paper with corn sizes of about 10 µm. Subsequently, these samples were polished further in an ion-milling system (IM4000, Hitachi High-Technologies Europe GmbH), and are denoted as ion-milling cross-sections (IM).

## Acknowledgements

The authors would like to express their sincere gratitude to Werner Stracke for his expert support in SEM sample preparation. Further the authors' appreciation also goes to Marco Nimbler for preparing some of the PC electrodes and Philip Daubinger for his valuable contributions for proof reading. The European Union's Horizon 2020 Research & Innovation program is thanked for funding the SOLiDIFY project (Grant Agreement No. 770142). Open Access funding enabled and organized by Projekt DEAL.

## Conflict of Interests

The authors declare no conflict of interest.

## Data Availability Statement

The data that support the findings of this study are available from the corresponding author upon reasonable request.

**Keywords:** 3D electrode architecture • aqueous processing • carbon current collector • high-loading cathodes • lithium-ion battery

- [1] J. B. Goodenough, K.-S. Park, *J. Am. Chem. Soc.* **2013**, *135*, 1167.
- [2] J. Janek, W. G. Zeier, *Nat. Energy* **2016**, *1*, 1167.
- [3] G. Crabtree, E. Kócs, L. Trahey, *MRS Bull.* **2015**, *40*, 1067.
- [4] S.-H. Park, P. J. King, R. Tian, C. S. Boland, J. Coelho, C. Zhang, P. McBean, N. McEvoy, M. P. Kremer, D. Daly, J. N. Coleman, V. Nicolosi, *Nat. Energy* **2019**, *4*, 560.
- [5] Z. Du, D. L. Wood, C. Daniel, S. Kalnaus, J. Li, *J. Appl. Electrochem.* **2017**, *47*, 405.
- [6] Y. Kuang, C. Chen, D. Kirsch, L. Hu, *Adv. Energy Mater.* **2019**, *9*, 1901457.
- [7] H. Zheng, J. Li, X. Song, G. Liu, V. S. Battaglia, *Electrochim. Acta* **2012**, *71*, 258.
- [8] L. S. Kremer, A. Hoffmann, T. Danner, S. Hein, B. Prifling, D. Westhoff, C. Dreer, A. Latz, V. Schmidt, M. Wohlfahrt-Mehrens, *Energy Technol.* **2020**, *8*, 1900167.
- [9] L. Neidhart, K. Fröhlich, N. Eshraghi, D. Cupid, F. Winter, M. Jahn, *Nanomaterials* **2022**, *12*.
- [10] P. Zhu, J. Han, W. Pfleging, *Nanomaterials* **2021**, *11*.
- [11] D. Parikh, T. Christensen, J. Li, *J. Power Sources* **2020**, *474*, 228601.
- [12] X. Zhang, Z. Ju, Y. Zhu, K. J. Takeuchi, E. S. Takeuchi, A. C. Marschilok, G. Yu, *Adv. Energy Mater.* **2021**, *11*, 2000808.
- [13] L. Hu, F. La Mantia, H. Wu, X. Xie, J. McDonough, M. Pasta, Y. Cui, *Adv. Energy Mater.* **2011**, *1*, 1012.
- [14] H. Sun, J. Zhu, D. Baumann, L. Peng, Y. Xu, I. Shakir, Y. Huang, X. Duan, *Nat. Rev. Mater.* **2019**, *4*, 45.
- [15] T. Hara, A. Konarov, I. Kurmanbayeva, Z. Bakenov, **2015**, <https://nur.nu.edu.kz/handle/123456789/891>. Accessed 31 May 2023.
- [16] P. Zhu, D. Gastol, J. Marshall, R. Sommerville, V. Goodship, E. Kendrick, *J. Power Sources* **2021**, *485*, 229321.
- [17] S. Jin, Y. Jiang, H. Ji, Y. Yu, *Adv. Mater.* **2018**, *30*, e1802014.
- [18] G. F. Yang, K. Y. Song, S. K. Joo, *J. Mater. Chem. A* **2014**, *2*, 19648.
- [19] M. Fritsch, G. Standke, C. Heubner, U. Langlotz, A. Michaelis, *J. Energy Storage* **2018**, *16*, 125.
- [20] J. Wang, M. Wang, N. Ren, J. Dong, Y. Li, C. Chen, *Energy Storage Mater.* **2021**, *39*, 287.
- [21] C. Chen, Y. Zhang, Y. Li, Y. Kuang, J. Song, W. Luo, Y. Wang, Y. Yao, G. Pastel, J. Xie, L. Hu, *Adv. Energy Mater.* **2017**, *7*, 1700595.
- [22] T. Wu, Z. Zhao, J. Zhang, C. Zhang, Y. Guo, Y. Cao, S. Pan, Y. Liu, P. Liu, Y. Ge, W. Liu, L. Dong, H. Lu, *Energy Storage Mater.* **2021**, *36*, 265.

- [23] Z. Zhao, M. Sun, W. Chen, Y. Liu, L. Zhang, N. Dongfang, Y. Ruan, J. Zhang, P. Wang, L. Dong, Y. Xia, H. Lu, *Adv. Funct. Mater.* **2019**, *29*, 1809196.
- [24] Y. Kuang, C. Chen, G. Pastel, Y. Li, J. Song, R. Mi, W. Kong, B. Liu, Y. Jiang, K. Yang, L. Hu, *Adv. Energy Mater.* **2018**, *8*, 1802398.
- [25] A. Benítez, Á. Caballero, E. Rodríguez-Castellón, J. Morales, J. Hassoun, *ChemistrySelect* **2018**, *3*, 10371.
- [26] A. Benítez, F. Luna-Lama, A. Caballero, E. Rodríguez-Castellón, J. Morales, *J. Energy Chem.* **2021**, *62*, 295.
- [27] D. W. Kim, W. Y. Jo, C. W. Park, S. M. Hwang, J. B. Yoo, Y.-J. Kim, *Electrochim. Acta* **2020**, *341*, 135936.
- [28] M. Hofmann, F. Nagler, M. Kapuschinski, U. Guntow, G. A. Giffin, *ChemSusChem* **2020**, *13*, 5962.
- [29] D. L. Wood, J. Li, C. Daniel, *J. Power Sources* **2015**, *275*, 234.
- [30] M. Hofmann, M. Kapuschinski, U. Guntow, G. A. Giffin, *J. Electrochem. Soc.* **2020**, *167*, 140512.
- [31] M. Hofmann, M. Kapuschinski, U. Guntow, G. A. Giffin, *J. Electrochem. Soc.* **2020**, *167*, 140535.
- [32] A. Kukay, R. Sahore, A. Parejya, W. B. Hawley, J. Li, D. L. Wood, *J. Colloid Interface Sci.* **2021**, *581*, 635.
- [33] M. Hofmann, F. Nagler, U. Guntow, G. Sextl, G. A. Giffin, *J. Electrochem. Soc.* **2021**, *168*, 60511.
- [34] P. Zhu, P. R. Slater, E. Kendrick, *Mater. Des.* **2022**, *7*, 111208.
- [35] D. Aurbach, E. Zinigrad, Y. Cohen, H. Teller, *Solid State Ionics* **2002**, *148*, 405.
- [36] K. N. Wood, M. Noked, N. P. Dasgupta, *ACS Energy Lett.* **2017**, *2*, 664.
- [37] P. Bai, J. Li, F. R. Brushett, M. Z. Bazant, *Energy Environ. Sci.* **2016**, *9*, 3221.
- [38] P. Daubinger, M. Göttlinger, S. Hartmann, G. A. Giffin, *Batteries & Supercaps* **2023**, *6*, 144.
- [39] D. Lin, Y. Liu, Y. Cui, *Nat. Nanotechnol.* **2017**, *12*, 194.
- [40] J. Illig, M. Ender, T. Chrobak, J. P. Schmidt, D. Klotz, E. Ivers-Tiffée, *J. Electrochem. Soc.* **2012**, *159*, A952–A960.
- [41] M. Steinhauer, T. Diemant, C. Heim, R. J. Behm, N. Wagner, K. A. Friedrich, *J. Appl. Electrochem.* **2017**, *47*, 249.
- [42] M. Gaberscek, J. Moskon, B. Erjavec, R. Dominko, J. Jamnik, *J. Power Sources* **2008**, *11*, A170.
- [43] Q.-A. Huang, Y. Shen, Y. Huang, L. Zhang, J. Zhang, *Electrochim. Acta* **2016**, *219*, 751.
- [44] V. Ovejas, A. Cuadras, *Batteries* **2018**, *4*, 43.
- [45] F. Schipper, M. Dixit, D. Kovacheva, M. Taliander, O. Haik, J. Grinblat, E. M. Erickson, C. Ghanty, D. T. Major, B. Markovsky, D. Aurbach, *J. Mater. Chem. A* **2016**, *4*, 16073.
- [46] N. Ogihara, Y. Itou, T. Sasaki, Y. Takeuchi, *J. Phys. Chem. C* **2015**, *119*, 4612.
- [47] W. Weppner, R. A. Huggins, *J. Electrochem. Soc.* **1977**, *124*, 1569.
- [48] A. M. Boyce, D. J. Cumming, C. Huang, S. P. Zankowski, P. S. Grant, D. J. L. Brett, P. R. Shearing, *ACS Nano* **2021**, *15*, 18624.
- [49] P.-P. R. M. L. Harks, C. B. Robledo, C. George, C. Wang, T. van Dijk, L. Sturkenboom, E. D. W. Roesink, F. M. Mulder, *J. Power Sources* **2019**, *441*, 227200.
- [50] F. J. Günter, N. Wassiliadis, *J. Electrochem. Soc.* **2022**, *169*, 30515.
- [51] M. J. Lain, J. Brandon, E. Kendrick, *Batteries* **2019**, *5*, 64.

Manuscript received: February 22, 2023

Revised manuscript received: May 1, 2023

Accepted manuscript online: May 16, 2023

Version of record online: June 2, 2023